Contents lists available at ScienceDirect

Applied Catalysis B: Environment and Energy

Low-valent cation doping and leaching to construct single-atom Cu decorated Cu-ZnIn$_2$S$_4$ with multiple defects for boosting photocatalytic H$_2$ evolution

Xuehua Wang [a], Tianyu Shi [a], Xianghu Wang [b], Guicun Li [a], Lei Wang [b], Jianfeng Huang [c], Alan Meng [b,*], Zhenjiang Li [a,*]

[a] College of Materials Science and Engineering, Qingdao University of Science and Technology, Qingdao 266042, Shandong, PR China
[b] Key Laboratory of Optic-electric Sensing and Analytical Chemistry for Life Science, MOE. College of Chemistry and Molecular Engineering, Qingdao University of Science and Technology, Qingdao 266042, Shandong, PR China
[c] School of Material Science and Engineering, International S&T Cooperation Foundation of Shaanxi Province, Xi'an Key Laboratory of Green Manufacture of Ceramic Materials, Shaanxi University of Science and Technology, Xi'an 710021, Shananxi, PR China

ARTICLE INFO

ABSTRACT

It is a promising means to enhance photocatalytic activity by ions doping, single-atom decoration, and vacancies introducing, yet a simple approach to realize their simultaneous appearance in one material remains a great challenge hitherto. Herein, an original strategy of low-valent cation doping and leaching is developed to construct Cu single atom (Cu SAs)-decorated and monovalent Cu ion (Cu$^+$)-doped ZnIn$_2$S$_4$ photocatalyst (RCu-ZIS) with multiple defects. The Cu doping atoms and Cu/In/S vacancies clusters induce electron-poor zones, meanwhile, S vacancies and isolated Cu SAs result in electron-rich regions, thus forming some local electric field with different states of charge, which can act as electron-accepting and donating centers accelerating the transfer and separation of photocarriers. The optimized RCu-ZIS delivers a high visible-light-driven H$_2$ evolution activity of 70.58 mmol·g^{-1}·h^{-1} with an AQE of 12.24% at 420 nm. This work opens up an all-in-one modification strategy on redounding photocatalytic activity through rational structural fine-tuning.

1. Introduction

Under the context of pursuing carbon-neutral technology, photocatalytic H$_2$ production offers a compelling approach for transforming inexhaustible solar energy into clean hydrogen and realizing zero-emission renewable energy evolution [1–3]. In this context, the study on efficient H$_2$ evolution photocatalysts has aroused widespread concern among worldwide researchers. In the past decades, tremendous attempts including single-atom decorating [4–6]], cation or anion doping [7–9], morphology or structure modulating [10–12], homo- or heterojunction constructing [13–15], and cocatalyst loading [16,17], have been developed to scale up H$_2$ evolution activity. Among the various modification strategies, single-atom decorated photocatalysts have been closely watched in recent years. In a single-atom involved photocatalytic system, the isolated reactive centers can not only create an increased number of active sites for photocatalytic reactions but also broaden the light-harvesting range and elevate the charge

separation/transfer efficiency [18]. Albeit with many merits, single-atom with large surface energy are rather easy to aggregate into clusters even nanoparticles, which brings great difficulties in stabilizing and maintaining the atomically dispersed isolated atoms on supports [19]. Therefore, it is still a great challenge to develop an effective and robust strategy for obtaining stabilized single-atom decorated photocatalysts.

Besides single-atom decorating, cation doping is also one of the most popular methods to modify photocatalysts. As revealed, impurity atoms with different sizes and valence states would induce evident changes in local surface microstructure, electronic band structure, and chemical properties of intrinsic photocatalyst [20], which could contribute to distinct influences on photocarriers separation and transfer efficiency [21]. Similar to impurity atoms, cation/anion vacancy defects are another kind of point defect that could affect photocatalytic activity by introducing defect levels to influence the generation, separation, and transfer behavior of photocarriers. More coincidentally, under the

---

influence of dopant atoms, lattice self-adaptation that some adjacent original atoms escape from the lattice to create cation/anion vacancy defects can always occur [22]. Recently, Liu's group reported a Cu^{2+} doped $ZnIn_2S_4$ with self-adapting S vacancy, which exhibited an enhanced H_2 evolution performance of 9.8647 $mmol \cdot g^{-1} \cdot h^{-1}$ [23]. It can be inferred that if Cu^+ with a larger radius (0.077 nm) and lower valence state than that of Cu^{2+} were doped in $ZnIn_2S_4$, a novel $ZnIn_2S_4$-based photocatalyst with richer vacancy concentration would be obtained for pursuing electrical neutrality and structural stability. Nor is this all, if a portion of Cu^+ shackled in the crystal lattice of $ZnIn_2S_4$ can be leached to become isolated Cu atoms, more newfangled structural/property changes would occur on $ZnIn_2S_4$. Such low-valent cation doping and leaching strategy could collect the merits of single-atom decoration, cation doping, and defect constructing simultaneously, and is hoped to realize a significant photocatalytic activity enhancement. However, this kind of all-in-one modification strategy has not been tried and reported yet.

Herein, as a proof of the above design, a low-valent cation doping and leaching strategy was developed for constructing Cu SAs-decorated and Cu^+-doped $ZnIn_2S_4$ photocatalyst with S vacancies and Cu/In/S vacancies clusters. During the Cu^+ doping process, S vacancies were formed to suit the structure and charge imbalance. When Cu-ZIS was immersed in $NaBH_4$, the superficial doping Cu^+ was reduced preferentially and dissociated from the lattice of RCu-ZIS to become the isolated Cu SAs, which further resulted in a higher concentration of S vacancies even vacancies clusters in RCu-ZIS. Compared to the original ZIS, the optimized RCu-ZIS photocatalyst achieves an H_2 production rate of 70.58 $mmol \cdot g^{-1} \cdot h^{-1}$ with an AQE of 12.24% at 420 nm. Experimental results and DFT calculations unveiled that the synergistic effect among isolated Cu SAs, Cu doping atoms, S vacancies, and Cu/In/S vacancies clusters induced local electric fields in RCu-ZIS, which accelerated the transfer and separation efficiencies of photocarriers. This work paves a new route for developing highly efficient photocatalytic materials.

2. Experimental section

2.1. Materials

$Zn(CH_3COO)_2 \cdot 2H_2O$, CuCl, ethanol, N, N-dimethylformamide, ethylene glycol, NaOH, and ascorbic acid were purchased from Sinopharm Chemical Reagent Co. LTD. $InCl_3$, $NaBH_4$, and thioacetamide (TAA) were obtained from Shanghai Macklin biochemical technology Co. LTD. All chemicals were used without further purified in the experiments.

2.2. Photocatalyst preparation

2.2.1. Cu^+ doping in $ZnIn_2S_4$

Cu^+ was doped in $ZnIn_2S_4$ through a solvothermal process. In a typical procedure, 0.5 mmol of $Zn(CH_3COO)_2 \cdot 2H_2O$, 1 mmol of $InCl_3$, and a certain amount of CuCl (0.02, 0.03, 0.04, 0.05, and 0.06 mmol) were added into a mixture solution containing 15 mL of ethylene glycol and 15 mL of N, N-dimethylformamide to obtain a homogeneous aqueous solution under stirring. Then, 4 mmol of thioacetamide was added to the above solution and stirred for another 0.5 h. Subsequently, the aqueous solution was transferred to 100 mL of Teflon liner and heated at 180 °C for 10 h. After cooling to room temperature, the precipitates were separated by centrifugation and washed several times using deionized water and ethanol. Finally, the collected solid was dried at 60 °C for about 4 h and labeled as Cu-ZIS. In the following, unless otherwise specified, Cu-ZIS represents the photocatalyst synthesized by adding 0.04 mmol of CuCl. For comparison, the pristine $ZnIn_2S_4$ (named ZIS) was synthesized via the same procedure of Cu-ZIS without adding CuCl.

2.2.2. Cu^+ leaching from Cu-ZIS

In a typical procedure, 100 mg of the synthesized Cu-ZIS was dispersed in 20 mL of NaOH solution (0.2 $mol \cdot L^{-1}$) containing $NaBH_4$ (0.1 $mol \cdot L^{-1}$) by ultrasonic for 1 h and stirring for 6 h. Thereafter, the suspension was separated by centrifugation and washed several times using deionized water until the supernatant reached neutral. Finally, the obtained sediment was dried in a vacuum drying oven at 60 °C for about 4 h. The final product was named RCu-ZIS. In the subsequent description, RCu-ZIS refers to the sample prepared by doping 0.04 mmol of Cu-ZIS.

2.3. Photocatalytic H_2 evolution measurements

Photocatalytic H_2 evolution reaction was carried out in a Pyrex reaction cell connected with a closed gas circulation system (Labsolar-6A, Beiiing Perfectlight Technology Co., Ltd.). Typically, 10 mg of the synthesized photocatalyst was dispersed in a 100 mL aqueous solution containing ascorbic acid (0.1 M) as a sacrificial agent. The dispersion was then added into the reaction cell and vacuumed for at least 0.5 h to remove the mixed air. Before the photocatalytic reaction, the light source (300 W Xe lame equipped with a 420 nm cut-off filter) was preheated for 0.5 h to ensure the stability of the light output. During the photocatalytic experiment, high-purity argon was used as the carrier gas, the temperature of the reaction solution was kept at 5 °C, and a magnetic stirrer was fixed under the reaction cell to avoid the settlement of the photocatalyst. The evolved H_2 was analyzed every 30 min on GC7900 gas chromatography (Techcomp). Apparent quantum efficiency (AQE) was tested following a similar procedure of photocatalytic H_2 evolution test except that the 420 nm cut-off filter was successively replaced by a 380, 420, 500, and 600 nm bandpass filter.

2.4. Materials characterizations

The crystal phases of photocatalysts were characterized by X-ray diffraction (XRD, Bruker, D8 ADVANCE) with Cu Kα ($\lambda = 1.5406$ Å, 40 kV, 20 mA) at a scanning speed of 5° min^{-1} and 2 theta range from 10° to 90°. The microstructures and morphologies of photocatalysts were observed by scanning electron microscopy (SEM, SU8010) and transmission electron microscopy (TEM, JEOL JEM-F200) equipped with atomic resolution analytical microscope (TecnaiG2F20 S-TWIN) for EDX spectra characterization. Atomic-resolution high-angle annular dark-field scanning transmission electron microscopy (HAADF-STEM) was carried out on JEM-ARM200F NEOARM. X-ray photoelectron spectra (XPS) and X-ray excited Auger electron spectra (XAES) were obtained from X-ray photoelectron spectrometer (Shimadzu AXIS SUPRA) with an Al Kα X-ray source (hv = 1486.6 eV). The local chemical environment of Cu atoms in the as-prepared photocatalysts was studied by the synchrotron X-ray spectroscopic (XAS) measurements performed on Beijing Synchrotron Radiation Facility (BSRF). Ultraviolet photoelectron spectroscopy (UPS) was carried out on the same system with XPS under the He I excitation Line (21.22 eV). An electron paramagnetic resonance spectrometer (EPR, JEOL JES-FA200) was adopted to identify the defect information in the synthesized photocatalysts (microwave frequency of 9065.41 MHz, 298 K in the air). UV–vis spectrophotometer (PerkinElmer Lambda 750 S) was used to investigate the light-responsive behavior of photocatalysts using $BaSO_4$ as the standard reference. F-4600 spectrofluorometer was used to detect the recombination of photocarriers (375 nm excitation wavelength). Time-resolved PL spectra were carried out on HORIBA Delta Pro under 375 nm excitation.

2.5. Electrochemical and photoelectrochemical characterizations

Transient photocurrent response, electrochemical impedance spectroscopy (EIS), and Mott-Schottky tests were carried out on a standard three-electrode cell (CHI-660E, Shanghai, China). The counter electrode and reference electrode were Pt-electrode and Ag/AgCl electrodes,

respectively, and the electrolyte was 0.5 M of Na_2SO_4. The working electrode was fabricated by daubing the mixed N-methyl-2-pyrrolidone paste including photocatalyst, carbon black, and polyvinylidene fluoride (in a mass ratio of 8:1:1) on a piece of pre-cleaned graphite sheet collector (1×1 cm^2).

2.6. DFT computational details

The first-principle calculations are performed to reveal the mechanism by using the Vienna ab initio simulation package [24,25]. The program has the projected enhancement wave pseudopotential [26] and the generalized gradient approximation of Perdew, Burke, and Enzzerhof (PBE) exchange-correlation functional [27], which is used to optimize the structure and obtain the free energy of all structures. The cutoff energy of the plane waves basis set is 500 eV and a Monkhorst-Pack mesh of $3 \times 3 \times 1$ is used in K-sampling in the adsorption energy calculation. The electronic self-consistent iteration is set to 10^{-5} eV, and the positions of all of the atoms are fully relaxed until the residual force on each atom is below 0.02 eV Å$-$ 1.15 Å of vacuum layer along the z-direction is applied to avoid periodic interactions.

3. Results and discussion

### 3.1. Preparation, phase analysis, and density functional theory simulation

As shown in Scheme 1, initially, the Cu$^+$ source of CuCl was added in the N, N-dimethylformamide/ethylene glycol mixture containing $ZnCH_3COO_2$, $InCl_3$, and CH_3CSNH_2. The competing coordination between Cu$^+$ and Zn^{2+}/In^{3+} with S^{2-} during solvothermal reaction allows Cu$^+$ to enter the crystal lattice of $ZnIn_2S_4$ and obtain Cu-ZIS. In this process, S vacancies were formed to suit the structure and charge imbalance due to valence states and radii differences among Cu$^+$ (0.77 Å), Zn^{2+} (0.74 Å), and In^{3+} (0.8 Å). After that, when Cu-ZIS was immersed in NaBH$_4$ solution, H$^-$ with robust electron donating ability would attack Zn, In, and Cu atoms on the surface of Cu-ZIS to form the RCu-ZIS. Apparently, according to metal active order, the oxidizing ability among Zn^{2+}, In^{3+}, and Cu$^+$ are in the order of Cu$^+$ > In^{3+} > Zn^{2+}, which means that Cu$^+$ are more likely to get electrons and deviate from the regular lattice points of RCu-ZIS, becoming isolated Cu SAs. Meanwhile, some In^{3+} and Zn^{2+} would also be marginally reduced to form low valence In/Zn ions with decreased coordination ability to S atoms, which therefore results in a higher concentration of S vacancies even vacancies clusters in RCu-ZIS. The isolated Cu SAs, Cu doping atoms, S vacancies, and vacancies clusters could play different influences on the electronic structure of $ZnIn_2S_4$, and regulate the generation, transfer, and separation behavior of photocarriers universally.

X-ray powder diffraction (XRD) technique was carried out to determine the phase structure of the synthesized photocatalysts. As observed in Fig. 1a, Cu-ZIS and RCu-ZIS present almost consistent diffraction peaks with that in ZIS, suggesting that Cu$^+$ doping or leaching procedure cannot transform the crystal structure of ZIS significantly. From the enlarged picture of the circled region in Fig. 1a, the peak of the (006) plane in Cu-ZIS presents an obvious shift towards the high angle compared to that in ZIS, reflecting the lattice shrinking induced by doping Cu$^+$ with smaller radii than In^{3+} [28,29]. Further, the peak shift in RCu-ZIS gets more serious than that in Cu-ZIS, affirming the more significant lattice shrinking in RCu-ZIS. Raman spectra were recorded in Fig. 1b, in which the two peaks at 349.57 and 684.27 cm^{-1} in ZIS attributed to the second-order and third-order longitudinal optical mode (LO$_2$ and LO$_3$) of crystalline ZIS [30,31]. Cu-ZIS and RCu-ZIS exhibited attenuated Raman peaks compared to ZIS, suggesting the distorted structural symmetry induced by Cu$^+$ doping and leaching.

To gain an insightful observation of the atomic configuration in RCu-ZIS, atomic-resolution high-angle annular dark-field scanning transmission electron microscopy (HAADF-STEM) was carried out. Fig. 1c presents the atomic arrangement of the (001) plane of RCu-ZIS, in which the isolated bright spots can be observed clearly, and no obvious clusters and particles exist. The magnified image in Fig. 1d shows several regions of atoms missing, proving the formation of vacancy clusters (location "1") caused by the escape of Cu, In, and S atoms during the Cu$^+$ doping and leaching process. As observed from the crystal structure of $ZnIn_2S_4$ (Fig. S1), one Zn atom is located in the center of the regular In atoms hexameric ring. From Fig. 1e, the atomic arrangement that Zn atoms (atomic number: 30, dark spots) locate in the center of In atoms hexameric ring (atomic number: 49, bright spots) can be observed. In addition, the spot with smaller size and lower contrast than the In atom can be found at the In atom location (location "2"), which should be indexed to the Cu doping atom (atomic number: 29, dark spots) in the crystal lattice, meanwhile, In atom missing site without any bright spot can also be discerned in location "3". Interestingly, an isolated dark spot dissociating from the lattice can be found at location "4", corresponding to the isolated Cu SAs. As known from the above analysis, in addition to the isolated Cu SAs, there are three different defective sites including the Cu doping atoms, S vacancies, and Cu/In/S vacancies clusters existing in RCu-ZIS.

To reveal their respective action on electron distribution and photocatalytic activity, the charge density distribution of RCu-ZIS was calculated, and the optimized structure was displayed in Fig. S2. As observed in Fig. 1f and g, isolated Cu SAs, Cu doping atoms, S vacancy, and Cu/In/S vacancies cluster have obvious influences on charge distribution. More clearly, Fig. 1h displays the electron localization function (ELF) corresponding to the slice of location "2" in the bulk RCu-ZIS crystal. As observed, the Cu atom performs a more centralized electron cloud density than the In atom, but the electronic density of S atoms
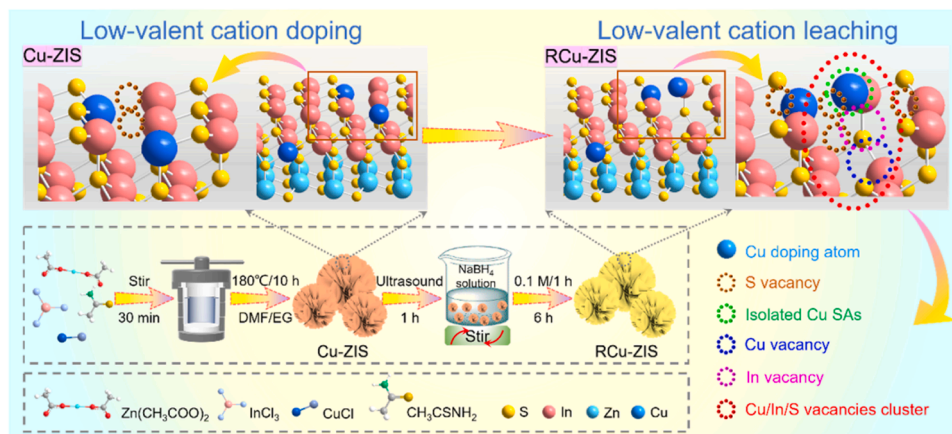
Scheme 1. Schematic illustration of the fabrication procedure of Cu-ZIS and RCu-ZIS.
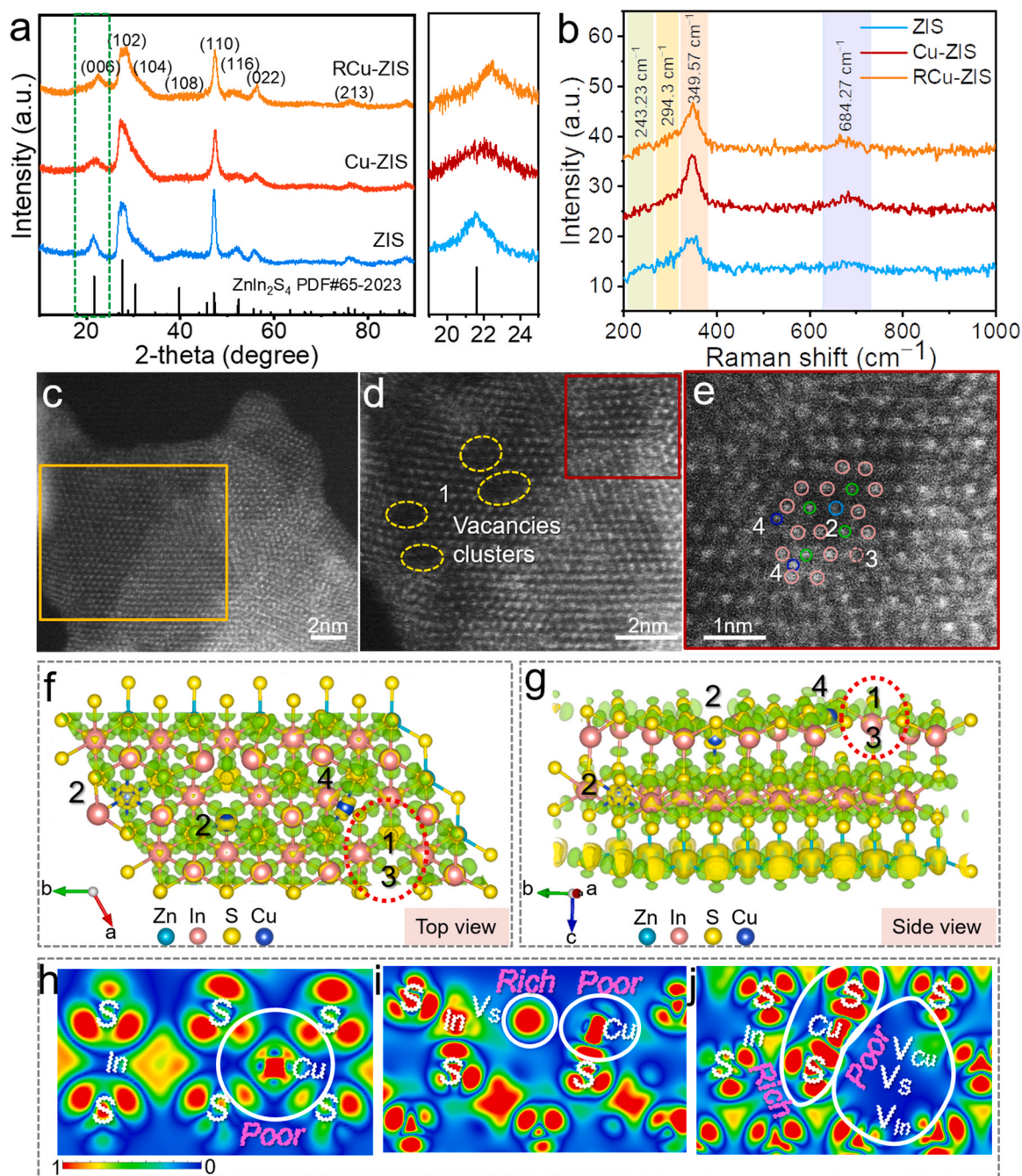
Fig. 1. (a) XRD pattern and (b) Raman spectra of ZIS, Cu-ZIS, and RCu-ZIS. (c-e) HAADF-STEM images of RCu-ZIS. Zn, In, and Cu atoms are circled by green, red, and blue solid circles, respectively. In vacancy and isolated Cu SAs are circled by the dotted red and black-blue solid circle, respectively. (f) Top and (g) side views of the charge density distribution of RCu-ZIS with green and yellow represent positive and negative electron density isosurfaces (0.007e/bohr3), respectively. (h-l) The electron localization function (ELF) of RCu-ZIS corresponding to different slice locations in (f, g), and Vs, V_{Cu}, and V_{In} represent the S vacancies, Cu vacancies, and In vacancies, respectively.

around Cu atoms exhibited an evident decrease than that around In atoms. Such obversion is related to the weaker electron-donating ability of Cu than that of In (electronegativity: Cu (1.99) > In (1.78)). More importantly, the slight electron-poor zone around Cu atoms can act as photogenerated electron trapping centers for charge balance, thus contributing to the effective separation of photocarriers [32]. Fig. 1i shows the ELF image of location "2" on the surface of RCu-ZIS. It can be observed that an obvious electrons cloud shrink occurs on the Cu doping atoms, but an intense electron-rich region with net negative charge distribution occurs on the S vacancy location, further revealing that the Cu doping atoms can act as electron traps, while S vacancies can serve as

effective electrons donors enriching the concentration of photogenerated electrons. As shown in Fig. 1j (the ELF image corresponding to location "4"), the isolated Cu SAs result in an obvious electron density increase over adjacent S atoms, and Cu/In/S vacancies induce a significant electron-poor zone, revealing the strong ability of vacancies clusters as electrons trapping centers for more efficient photocarriers separation. Through the above analysis, we can conclude that the isolated Cu SAs, Cu doping atoms, S vacancies, and Cu/In/S vacancies clusters result in some local electric field with different states of charge in RCu-ZIS, which can act as electron-accepting or donating centers accelerating the transfer and separation rate of photocarriers

coordinately, and inevitably result in an obvious improvement in photocatalytic H$_2$ evolution performance.

3.2. Morphology, microstructure, and composition study

The morphology and structure of the as-synthesized photocatalyst were characterized using scanning electron microscopy (SEM), transmission electron microscopy (TEM), and high-resolution transmission electron microscopy (HRTEM). As observed in Fig. S3, ZIS, Cu-ZIS, and RCu-ZIS all presented the particular flower-like micro-sphere structure composed of numerous ultra-thin nanosheets, which can favor the exposure of active sites and the utilization of incident light [30]. Such identical structures among ZIS, Cu-ZIS, and RCu-ZIS revealed that Cu$^+$ doping and leaching cannot destroy the integral micro-structure of ZIS. TEM images shown in Fig. 2a, d, and g reveal identical results with SEM. From the HRTEM image of ZIS (Fig. 2b and c), the lattice fringes with a
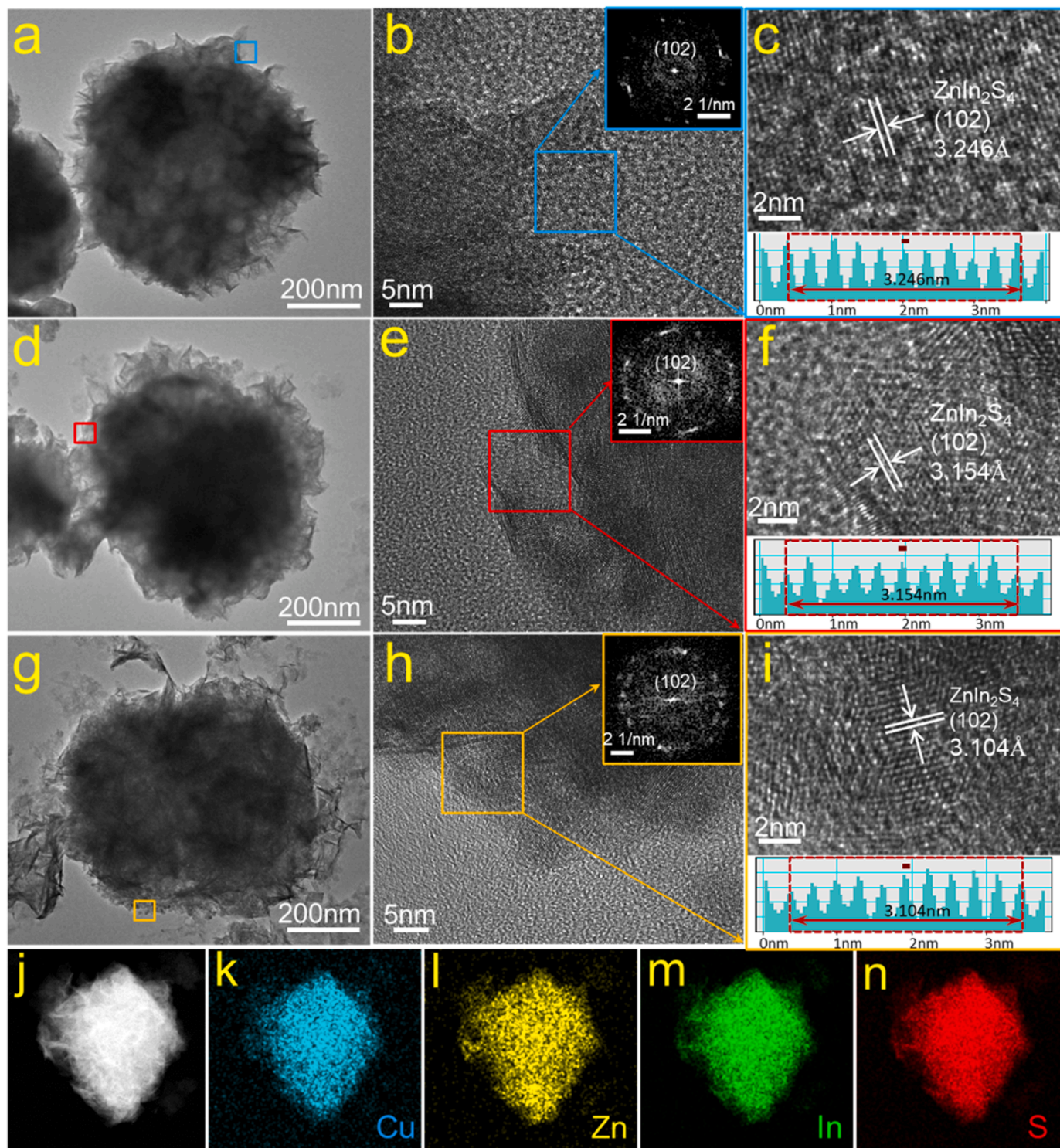

Fig. 2. (a-c) TEM, HRTEM and FFT (inset) of ZIS. (d-f) TEM, HRTEM and FFT (inset) of Cu-ZIS. (g-i) TEM, HRTEM and FFT (inset) of RCu-ZIS. (j-n) STEM image and element distribution mapping in RCu-ZIS.

plane spacing of 3.246 Å can be distinguished, which can be assigned to the (102) plane of hexagonal $ZnIn_2S_4$. As observed in the fast Fourier transformation (FFT) image inserted in Fig. 2b, the clear polycrystalline ring composed of distinct diffraction spots can be detected, revealing the good crystallinity of ZIS. Fig. 2e and f display the HRTEM of Cu-ZIS, in which a slightly narrower (102) plane spacing of 3.154 Å can be observed, which should be attributed to that Cu^+ doped in the lattice of ZIS by replacing In^{3+} with larger radii, and the competition coordination between Cu^+ and Zn^{2+}/In^{3+} with S^{2-} compress the bond length in Cu-ZIS, and induce local lattice shrink [33]. Energy-dispersive X-ray spectroscopy (EDX) and element-distributing spectra over Cu-ZIS shown in Fig. S4 display the evenly distributed Cu, Zn, In, and S, preliminarily proving the successful doping of Cu^+ in ZIS. Furtherly, a slightly decreased crystallinity of Cu-ZIS can be discerned from the FFT image inserted in Fig. 2e. As observed in the HRTEM of RCu-ZIS (Fig. 2 h and i), a further narrowed (102) plane spacing of 3.104 Å can be measured. Meanwhile, the diffraction spots are vaguer compared with those in Cu-ZIS, revealing the decreased crystallinity induced by $NaBH_4$ reduction. It can be speculated that the reduction process could remove a part of atoms (such as Cu and In) from the surface of Cu-ZIS, thus leading to

the decreased order degree of atomic arrangement. Fig. S5 presents the EDX spectra of RCu-ZIS, as displayed, Zn, In, S, and Cu elements can be detected simultaneously, and their distribution in RCu-ZIS micro-flower is relatively even (Fig. 2j-n), further revealing the uniform distribution of Cu atoms in RCu-ZIS.

Fig. 3a displays the EPR spectra of ZIS, Cu-ZIS, and RCu-ZIS. As exhibited, no distinct EPR signal can be detected over pristine ZIS. In comparison, Cu-ZIS displays an apparent EPR response at a g-value of 2.003, corresponding to the presence of S vacancies bounded with unpair electrons, which was induced by the unmatched size and charge between the doped Cu atoms and the substituted In atoms [34,35]. Conceivably, when Cu-ZIS was immersed in $NaBH_4$ solution, superficial Cu^+, Zn^{2+}, and In^{3+} would be reduced by the H^-, leading to the decreased valence state of Cu^+, Zn^{2+}, and In^{3+} (especially Cu^+). The valence state decrease means the decreased coordination ability of the S atoms, which could result in significant bond breaking, thus resulting in the generation of abundant dangling bonds and unpaired electrons on the S atoms. That's the reason that the EPR intensity of RCu-ZIS is higher than that of Cu-ZIS. The further enriched lone-pair electrons in RCu-ZIS are beneficial for the generation and separation of photogenerated
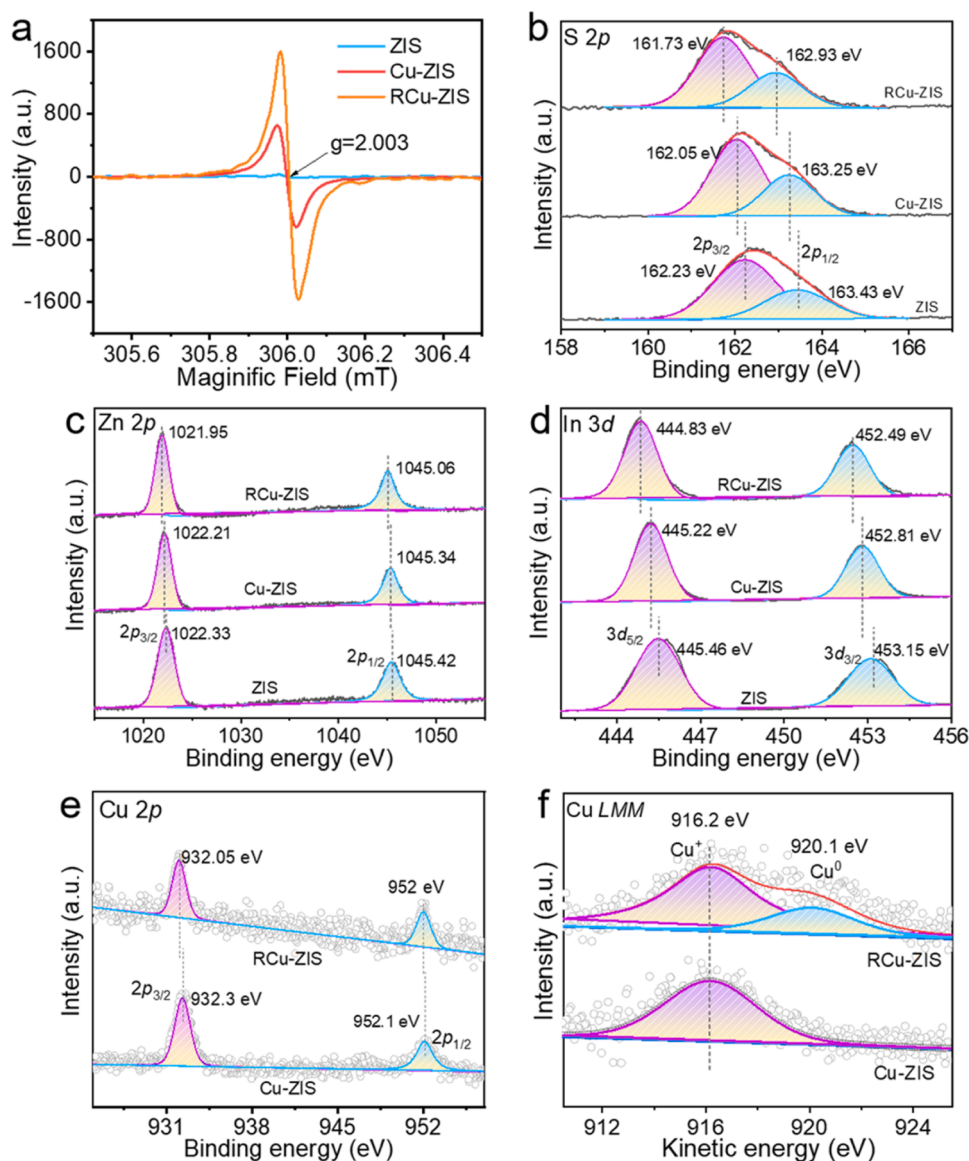
Fig. 3. (a) EPR spectra of ZIS, Cu-ZIS, and RCu-ZIS. b) S 2*p*, (c) Zn 2*p*, and (d) In 3*d* XPS spectra of ZIS, Cu-ZIS and RCu-ZIS. (e) Cu 2p and (f) Cu LMM of Cu-ZIS and RCu-ZIS.

carriers, thus contributing to photocatalytic H_2 evolution. To study the subtle chemical environment of Cu atoms in ZIS, X-ray photoelectron spectroscopy (XPS) was employed. Fig. S6 displays XPS survey spectra of ZIS, Cu-ZIS, and RCu-ZIS, in which Zn, In, and S elements were detected in all the tested photocatalysts, and Cu element was detected in Cu-ZIS and RCu-ZIS. For the detailed XPS spectra of ZIS, as observed in Fig. 3b, peaks situated at 162.23 and 163.43 eV can be well deconvoluted and correspond to S $2p_{3/2}$ and S $2p_{1/2}$ orbitals of S^{2-} in ZnIn$_2$S$_4$, respectively, two peaks located at 1022.33 and 1045.42 eV in Zn $2p$ spectra (Fig. 3c) can be assigned to Zn $2p_{3/2}$ and Zn $2p_{1/2}$ orbitals of Zn^{2+} in ZnIn$_2$S$_4$, respectively, and peaks at 445.46 and 453.15 eV in In $3d$ spectra (Fig. 3d) can be referred to In $3d_{5/2}$ and In $3d_{3/2}$ of In^{3+} in ZnIn$_2$S$_4$, respectively. The peak location of Zn, In, and S shows good consistency with reported literature [36,37], demonstrating the successful synthesis of ZIS photocatalyst. In comparison with ZIS, S $2p$ peaks in Cu-ZIS presented a visible peak shift to the lower binding energy region, revealing the increased electron cloud density around S atoms in Cu-ZIS, which should be ascribed to the generation of S vacancies induced by the embedding of Cu^+ with lower valence state and weaker coordinating ability. Meanwhile, the peak of Zn $2p$ and In $3d$ of Cu-ZIS show a distinct shift to the lower binding energy region, suggesting the higher density of electrons around Zn and In atoms in Cu-ZIS, which should also be the result of S vacancies [38,39]. It is interesting to sight that the binding energy shift of In $3d$ is greater than that of Zn $2p$, demonstrating that more S vacancies formed around In atoms [40]. For RCu-ZIS, the binding energy of S $2p$, Zn $2p$, and In $3d$ peaks present a further shift towards the lower binding energy zone, revealing the further enriched electron density over Zn and In atoms in RCu-ZIS. Such variation should be attributed to that NaBH$_4$ with an intense reducing effect donated electrons to Zn/In atoms, thus contributing to the slightly decreased valence state and coordination ability of Zn/In ions in RCu-ZIS, which results in the break of Zn-S and In-S chemical bonds, thereby further enriching S vacancies concentration in RCu-ZIS. The negatively shifted binding energy of S $2p$ in RCu-ZIS compared to that in Cu-ZIS also reveals the existence of rich S vacancies in RCu-ZIS [41]. Fig. 3e displays the Cu $2p$ spectra of Cu-ZIS and RCu-ZIS. As displayed, two peaks at 932.3 and 952.1 eV in Cu $2p$ spectra of Cu-ZIS can be observed, which can be assigned to Cu $2p_{3/2}$ and Cu $2p_{1/2}$ of Cu^+, respectively, in comparison, the peaks in RCu-ZIS presents slightly shift to the lower binding energy, revealing the existence of Cu species with lower valence state in RCu-ZIS. To further confirm the valence state of Cu in Cu-ZIS and RCu-ZIS, X-ray excited Auger electron spectra (XAES) of Cu *LMM* were conducted. As displayed in Fig. 3f, a singlet peak in Cu-ZIS centered at 916.2 eV can be indexed to the Cu^+ species. For RCu-ZIS, in addition to the peak of Cu^+, another peak located at 920.1 eV can also be deconvoluted to zero valence Cu, confirming that zero-valence Cu SAs were generated in RCu-ZIS under the reducing effect of NaBH$_4$ [42,43].

XPS and EDX quantification analysis as well as inductively coupled plasma-atomic emission spectrometry (ICP-AES) techniques were conducted to investigate the element content in ZIS, Cu-ZIS, and RCu-ZIS photocatalysts (Table S1-S3). As displayed, the atoms ratio of Zn : In in ZIS was determined to be 1:2.01 and 1:1.97 by XPS and ICP-AES respectively, which are nearly consistent with the theoretical stoichiometric ratio in ZnIn$_2$S$_4$ (1 : 2). For Cu-ZIS photocatalyst, the atom ratio of Cu : Zn was calculated to be 0.078:1, 0.067:1, and 0.034:1 by EDX, XPS, and ICP-AES, respectively. More importantly, with the advent of Cu, the content of In and S decreased, suggesting that the Cu atom entered the crystal lattice of ZIS by replacing a part of In atoms, and generated a certain amount of S vacancies (the concentration of S vacancies was determined to 2.78%). After NaBH$_4$ reduction, S vacancies concentration got more increased (3.63%), and the ratio of In element in RCu-ZIS was further decreased, suggesting that a part of In atoms in RCu-ZIS were reduced by NaBH$_4$ and divorced from the crystal structure of RCu-ZIS. Moreover, the ratio of Cu : Zn in RCu-ZIS (0.022:1) tested by ICP-AES is smaller than that in Cu-ZIS (0.034:1), suggesting that the whole Cu content in RCu-ZIS is decreased after NaBH$_4$ reducing, which

should be ascribed to that a part of Cu^+ doped in Cu-ZIS was reduced to zero-valence Cu and divorced from the lattice of Cu-ZIS. However, the ratio of Cu : Zn in RCu-ZIS tested by XPS (0.077:1) and EDX (0.081:1) is larger than that in Cu-ZIS (0.067:1 and 0.078:1, respectively), which suggests that the superficial Cu atom content in RCu-ZIS is higher than that in Cu-ZIS. Combined the EDX, XPS, and ICP-AES results, we can infer that a part of Cu doping atoms was reduced by NaBH$_4$ and dissociated from RCu-ZIS, and a handful of isolated Cu SAs were absorbed on the surface of RCu-ZIS.

X-ray absorption near edge structure (XANES) and extended X-ray absorption fine structure (EXAFS) techniques were further performed to verify the inherent existing state of Cu atoms in Cu-ZIS and RCu-ZIS at the atomic level. As can be seen from Fig. 4a, both the absorption edge of Cu-ZIS and RCu-ZIS in the Cu K-edge of the XANES patterns located near Cu$_2$S, suggesting the Cu atoms in a valence state of $+ 1$ were doped in ZIS crystal lattice, which corroborates the XPS results [44]. The coordination environment of Cu atoms in Cu-ZIS and RCu-ZIS were further confirmed by Fourier transforms of Cu K-edge EXAFS displayed in Fig. 4b. It is evident that the peak positions of Cu in Cu-ZIS and RCu-ZIS are very similar to that in Cu$_2$S, but different from that in Cu foil, indicating Cu-S bonding similar to that in Cu$_2$S formed in Cu-ZIS and RCu-ZIS. Interestingly, as shown in the enlarged R-space spectra, the first coordination peaks of Cu-S in RCu-ZIS display a slight shift to the larger R-space and become weaker than that in Cu-ZIS, suggesting the decreased coordination number of Cu in RCu-ZIS, which corresponds to the generation of zero-valence Cu atoms [45,46]. No apparent Cu-Cu bonding peak occurred in RCu-ZIS, indicating that the zero velenve Cu in RCu-ZIS existed in the form of isolated Cu SAs instead of clusters or nanoparticles [47]. As displayed in Fig. 4c, the Cu K-edge oscillation curves for Cu-ZIS and RCu-ZIS display remarkable differences in comparison with both Cu foil and Cu$_2$S, further excluding the existence of metallic Cu and Cu$_2$S [48]. EXAFS wavelet transform (WT) analysis was further applied to confirm the atomic dispersion of Cu atoms by providing both k- and R- space resolution (Fig. 4d-g). The wavelet transform plot of Cu-ZIS shows an intensity maximum at around 6 Å^{-1} (Fig. 4d), which is close to the intensity maximum of Cu$_2$S standard (Fig. 4f), confirming that Cu^+ doped in ZIS bonded with S atoms. By comparison, after reducing by NaBH$_4$, the intensity maximum in the wavelet transform plot of RCu-ZIS exhibits a slight extension towards the larger R+ α and K, but Cu-Cu coordination is not observed (Fig. 4g), proving the generation of atomically dispersed zero-valence Cu SAs in RCu-ZIS, which can be further verified from the first derivative curves of Cu K-edge XANES spectra (Fig. 4h) [47,49]. It can be observed that the fitted curves for Cu-ZIS, RCu-ZIS, Cu foil, and Cu$_2$S are in good agreement with the experimental data (Fig. 4i). According to the detailed fitting parameters listed in Table S4, the Cu-S coordination number (CN) of RCu-ZIS (4.0) is indeed smaller than that of Cu-ZIS (4.3), directly revealing that NaBH$_4$ reduction could reduce the valence state of Cu^+ in RCu-ZIS, that is, generating a small amount of isolated Cu SAs.

3.3. Band structure, optical and electrochemical properties study

To examine the electronic structure of RCu-ZIS, band structure and density of states (DOS) were calculated. As observed in Fig. 5a, the band gap of RCu-ZIS is 1.52 eV, narrower than that of the pristine ZIS (2.219 eV, Fig. S7 and Fig. S8). It is found that the conduction band minimum (CBM) of RCu-ZIS is mainly composed In $1s2p3d$ and S $2p$ orbitals, and the valence band maximum (VBM) is contributed by the orbital hybridization between S $2p$ and Cu $1s3d$ (Fig. 5a and Fig. S9). The orbitals hybridization near VBM not only raises the level of VBM but also results in some states passing through the Fermi level, suggesting the degenerated semiconductor characters with metallic conductive of RCu-ZIS [50]. Such unfilled energy states in VBM are relevant to the lower electron donating ability of Cu than that of Zn and In and can act as electronic acceptor states suppressing the undesirable recombination of photocarriers [51,52]. Moreover, two mid-gap energy states appear in
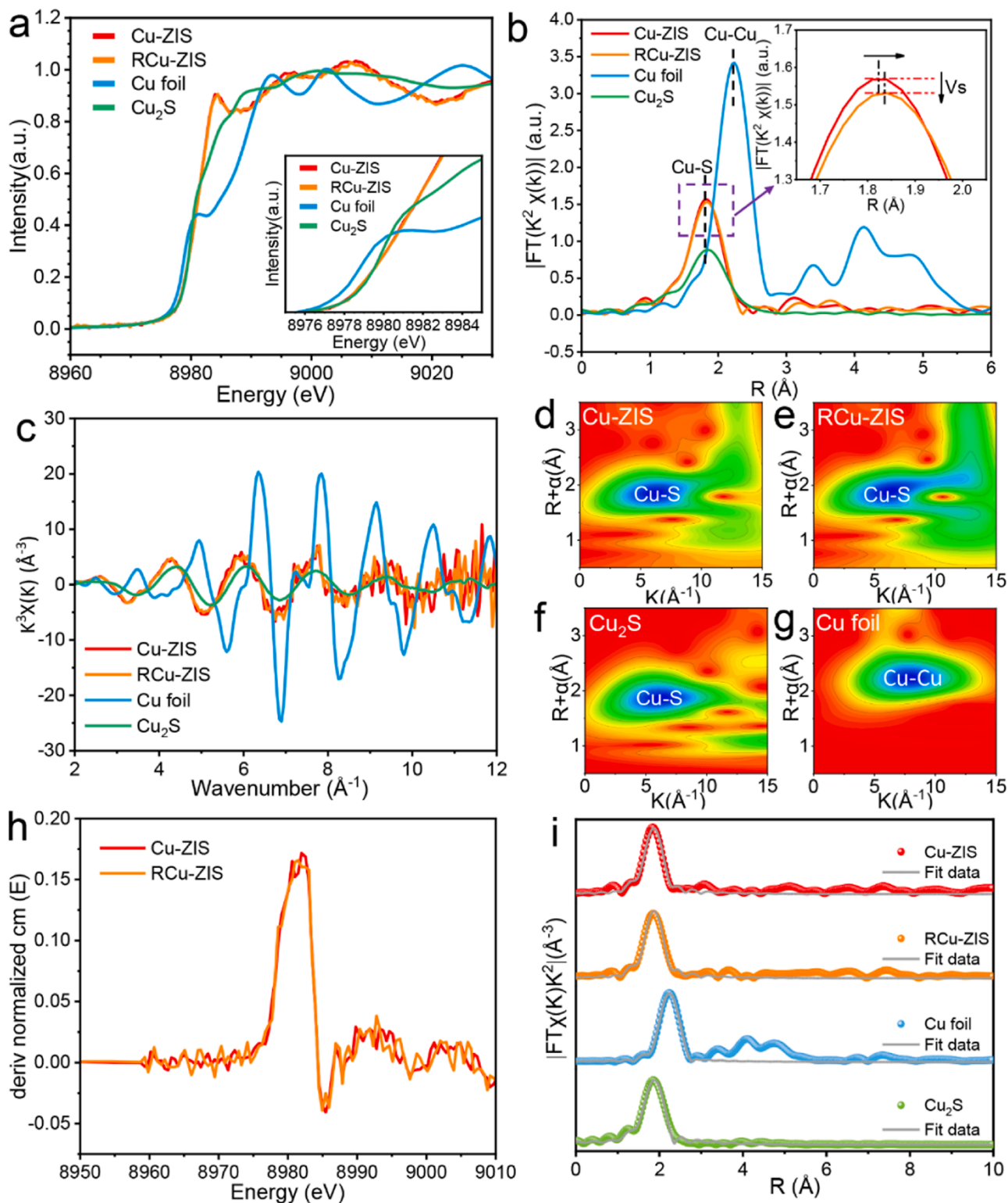
Fig. 4. (a) Cu K-edge XANES spectra of Cu-ZIS and RCu-ZIS compared with Cu^0 (Cu foil) and Cu^+ (Cu_2S) standards. (b) The magnitude of the Fourier transforms of k^3-weighted Cu K-edge EXAFS functions in Cu-ZIS, RCu-ZIS, Cu foil, and Cu_2S. (c) Cu K-edge extended EXAFS oscillation function of Cu-ZIS, RCu-ZIS, Cu foil, and Cu_2S. EXAFS wavelet transform (WT) contour plots of k^3-weighted v (k) signals of (d) Cu-ZIS, (e) RCu-ZIS, (f) Cu_2S, and (g) Cu foil. (h) First derivative curves of Cu K-edge XANES spectra of Cu-ZIS and RCu-ZIS. (i) Experimental and fitted R-space FT-EXAFS of Cu K-edge over Cu-ZIS, RCu-ZIS, Cu foil, and Cu_2S.

the band gap of RCu-ZIS, in which the mid-gap state near the CBM and composed by the hybridization of In and S orbitals originated from the acceptor level of S vacancies in RCu-ZIS [53], while another mid-gap state slightly away from CBM and arising from the hybridization of Cu, In, and S orbitals was related to the donor levels of Cu/In/S

vacancies clusters [54,55], which are responsible for the generation and separation of photogenerated electrons, respectively [56,57]. Fig. 5b displays the Kubelka-Munk function vs. the energy of incident light plots. By extending the straight-line section to the horizontal axis, the band gap of ZIS, Cu-ZIS, and RCu-ZIS can be determined to be 2.41, 1.61,
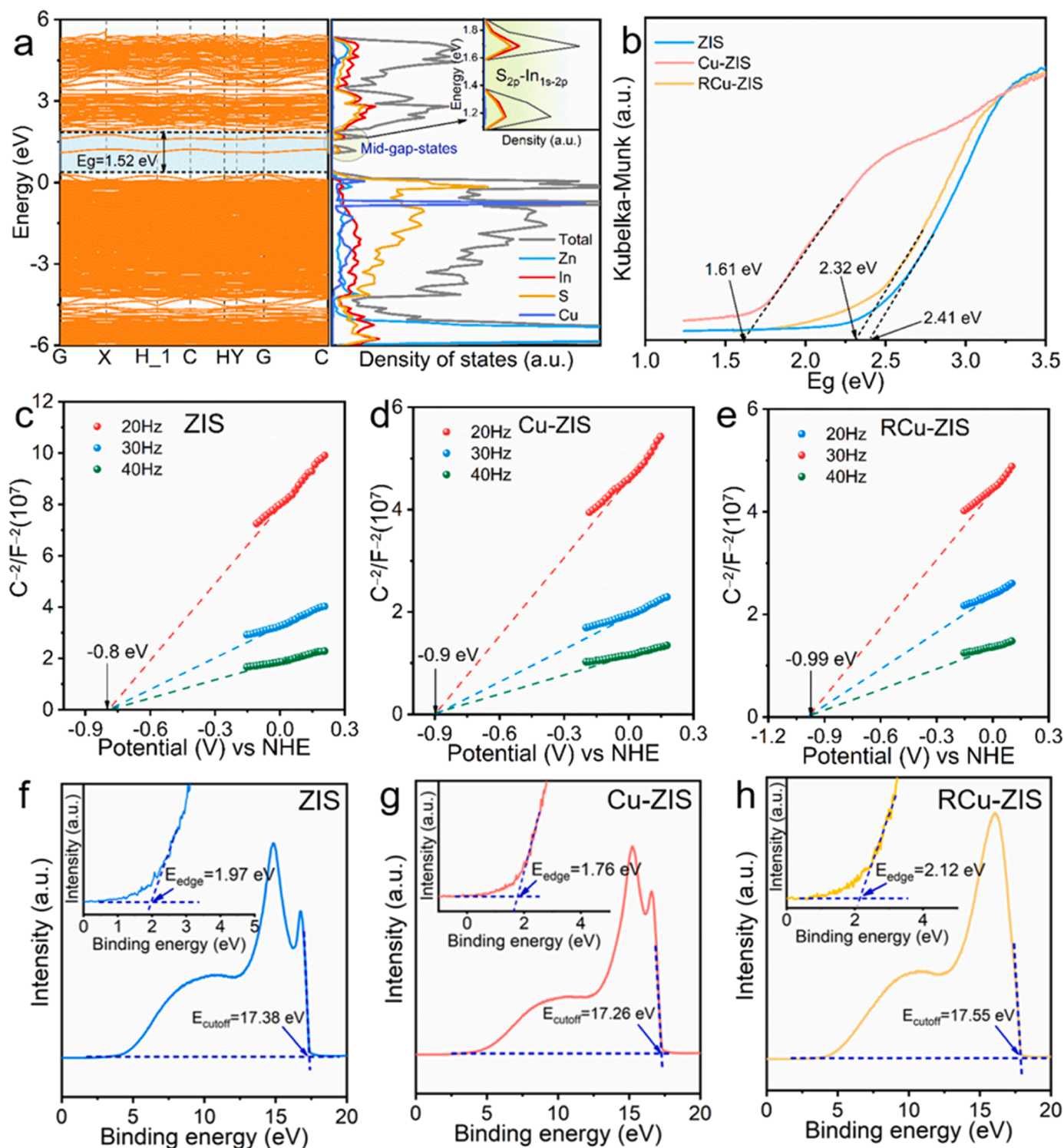
Fig. 5. (a) Band structure and DOS for RCu-ZIS calculated by DFT simulation. (b) Kubelka-Munk function vs. the energy of incident light plots of ZIS, Cu-ZIS, and RCu-ZIS. (c-e) Mott-Schottky (M-S) plots and (f-h) UPS spectra of ZIS, Cu-ZIS, and RCu-ZIS.

and 2.32 eV, respectively. According to the above theoretical calculation and reported results [58], Cu^+ doping mainly affects the valence band of ZIS, leading to the lifted VBM and narrower E_g of Cu-ZIS. While, cation vacancies and S vacancies can result in decreased VBM and increased CBM location, respectively [33,59], RCu-ZIS contains Cu doping atoms, Cu/In vacancies, and S vacancies concurrently, exhibiting a wider E_g than Cu-ZIS. From Mott-Schottky plots (Fig. 5c-e), the flat band potential of ZIS, Cu-ZIS, and RCu-ZIS was determined to be -0.8,

-0.9, and -0.99 eV (vs. NHE), respectively. Accordingly, their conduction band potentials (E_{CB}) were determined to be -1.0, -1.1, and -1.19 eV (vs. NHE), respectively [60]. Combining the band gap value determined from Fig. 5b, the valence band potentials (E_{VB}) of ZIS, Cu-ZIS, and RCu-ZIS were ascertained as 1.41, 0.5, and 1.13 eV vs. NHE, respectively. Besides that, the electronic structure of ZIS, Cu-ZIS, and RCu-ZIS was also determined through ultraviolet photoelectron spectroscopy (UPS) analysis. According to the calculation process shown in

Supporting Information, the valence band potentials of ZIS, Cu-ZIS, and RCu-ZIS were calculated to 0.96, 0.87, and 0.94 eV vs NHE, respectively, and their conduction band potentials were calculated to -1.45, -0.73 and -1.38 eV vs. NHE, respectively, which are close to the value intended from M-S plots.

The relative band alignment of ZIS, Cu-ZIS, and RCu-ZIS was intuitively depicted in Fig. 6a. In light of the altered electronic structure, the optical and electrochemical behavior of Cu-ZIS and RCu-ZIS would be changed compared to the pristine ZIS. Fig. 6b presents the UV–vis absorbance spectra of ZIS, Cu-ZIS, and RCu-ZIS. As shown, Cu-ZIS displays a greatly enhanced light absorption intensity in comparison to that of ZIS, besides that, the spectral responsive scope of Cu-ZIS is also wider than that of ZIS. Interestingly, RCu-ZIS appears a typical shoulder-like absorption in the range of 450–650 nm, implying that low energy states are present in the forbidden band, which is consistent with the

theoretical calculation results. Besides that, the visible light absorbance intensity of RCu-ZIS is weaker than that of Cu-ZIS, which should be ascribed to the generation of Cu/In/S vacancies leading to the broadened band gap of RCu-ZIS. As observed from Fig. 6c, the steady-state photoluminescence (PL) emission peak of Cu-ZIS presents a distinct quench compared to ZIS, suggesting the inhibited photocarrier recombination induced by Cu$^+$ doping [61]. Furtherly, it can be noticed that RCu-ZIS performs the lowest PL peak, which is related to the synergistic effect among isolated Cu SAs, Cu doping atoms, S vacancies, and Cu/In/S vacancies clusters contributed to the easy separation of photogenerated holes and electrons. As exhibited in Fig. 6d, all the tested photocatalysts display light-responsive behavior, and the photocurrent density changes periodically with the progress of switching light. Notably, RCu-ZIS exhibits the highest photocurrent density, further revealing the synergistic effect of isolated Cu SAs, Cu doping atoms, S
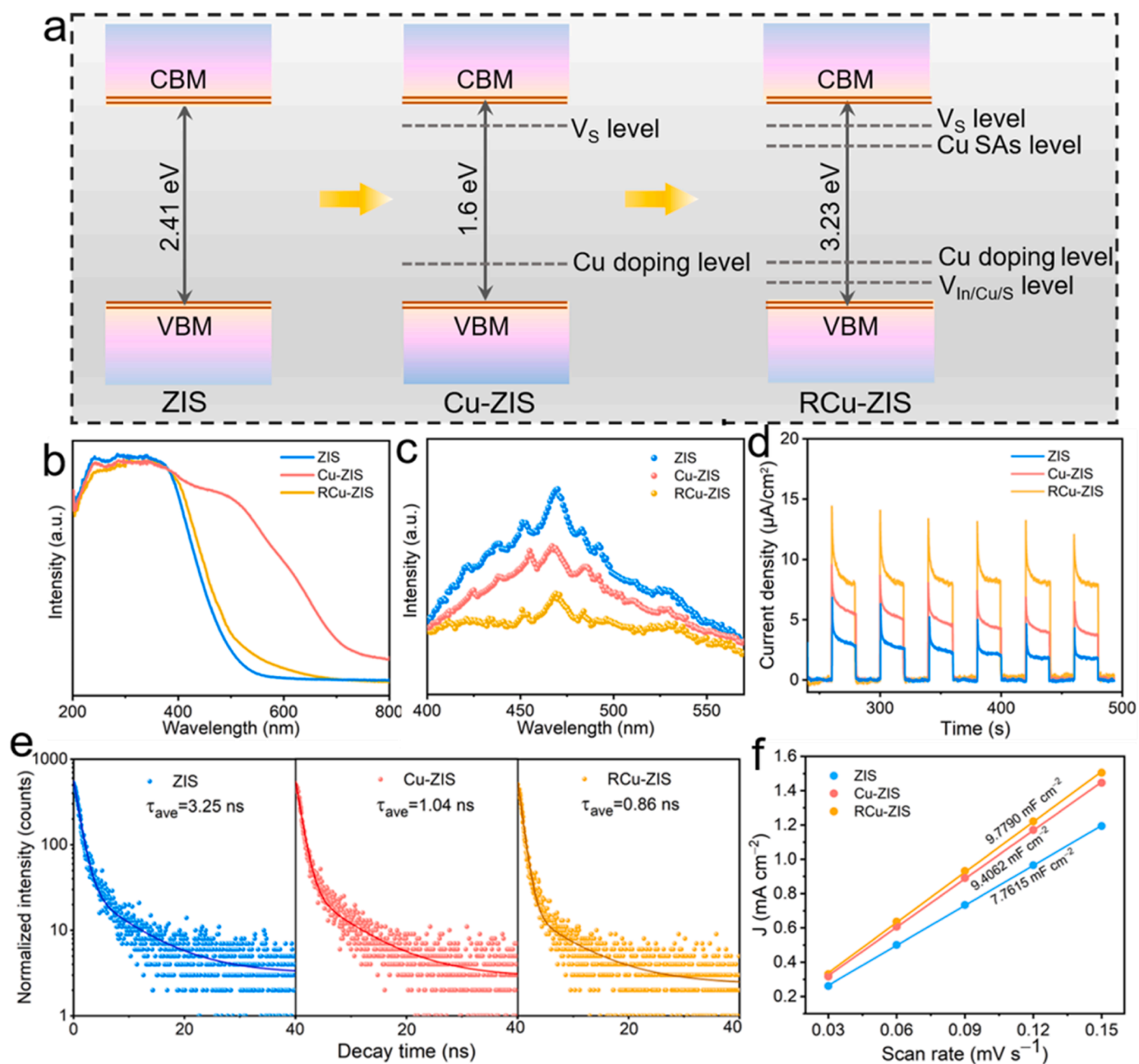

Fig. 6. (a) Band structure of ZIS, Cu-ZIS, and RCu-ZIS. (b) UV–vis absorbance spectra, (c) PL spectra, (d) transient photocurrent responsive plots with the light on/off cycles, (e) TRPL decay spectra (excitation at 375 nm), and (f) current density differences plotted against scan rates of ZIS, Cu-ZIS, and RCu-ZIS.

vacancies, and Cu/In/S vacancies clusters on boosting photocarrier transfer and separation efficiency. Fig. 6e displays time-resolved photoluminescence (TRPL) spectroscopy. Based on the triple exponential fitting equation of Fit $= A + B_1\exp\left(-\frac{t}{\tau_1}\right) + B_2\exp\left(-\frac{t}{\tau_2}\right) + B_3\exp\left(-\frac{t}{\tau_3}\right)$, the specific fitting results can be obtained (Table S5). Then, the average emission lifetime (τ_A) of ZIS, Cu-ZIS, and RCu-ZIS can be determined to be 3.25, 1.04, and 0.86 ns, respectively, according to the equation of τ_A

$= \frac{A_1\tau_1{}^2 + A_2\tau_2{}^2 + A_3\tau_3{}^2}{A_1\tau_1 + A_2\tau_2 + A_3\tau_3}$. The shorter lifetime of Cu-ZIS than ZIS indicates the more effective charge transfer and separation in Cu-ZIS owing to Cu doping atoms, meanwhile, the further shortened lifetime of RCu-ZIS than Cu-ZIS should be attributed to an additional decay channel that is opened through electron transfer from Cu-ZIS to isolated Cu SAs [62, 63]. Electrochemical surface area (ECSA) measurement is a useful means to obtain the active surface area data of a catalyst. Fig. 6f displays
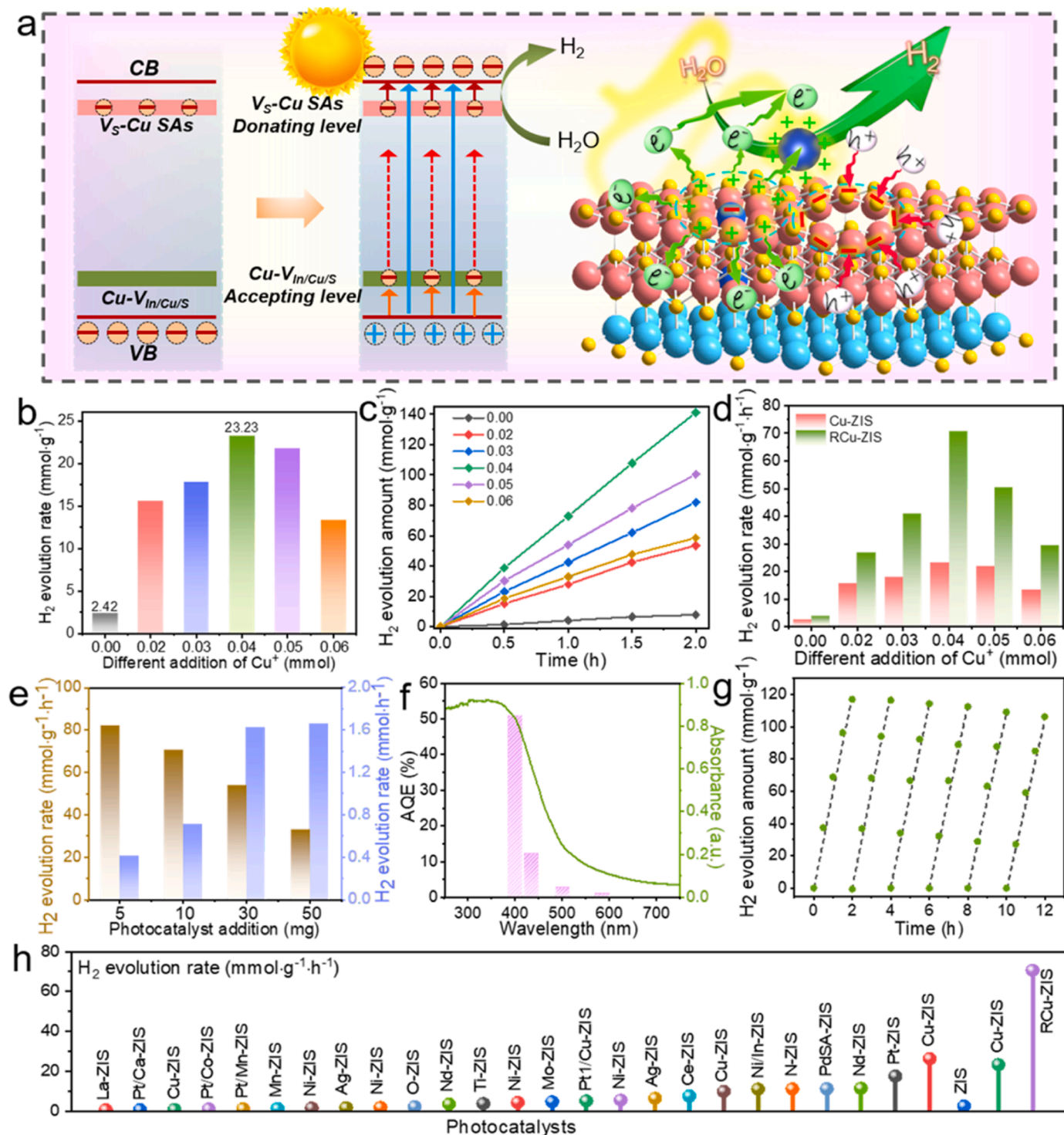
Fig. 7. (a) Photocatalytic H_2 evolution mechanism of ZIS and RCu-ZIS. H_2 evolution at different irradiation times over (b) Cu-ZIS and (c) RCu-ZIS with different Cu^+ doping amounts. (d) H_2 evolution rate comparison over Cu-ZIS and RCu-ZIS. (e) Comparison of H_2 evolution rate with different amounts of the optimized RCu-ZIS. (f) H_2 evolution AQE and UV–vis absorbance spectra of RCu-ZIS. (g) Cycling stability test over RCu-ZIS. (h) H_2 evolution rate for ZIS, Cu-ZIS, and RCu-ZIS in this work compared with representative recently reported photocatalysts.

the double-layer capacitance (C_{dl}) of ZIS, Cu-ZIS, and RCu-ZIS, which is in proportion to ECSA and measured by cyclic voltammetry (CV) measurements as a function of scan rates (Fig. S10). As observed, Cu-ZIS displays a larger C_{dl} value (9.4062 mF cm^{-1}) than that of ZIS (7.7615 mF cm^{-1}), while RCu-ZIS presents the greatest C_{dl} value of 9.7790 mF cm^{-1}, demonstrating that Cu$^+$ doping and leaching strategy can effectively increase the number of active sites on RCu-ZIS, which is one of the important factors for efficient photocatalytic activity [64]. Fig. S11 presents the EIS Nyquist plots of ZIS, Cu-ZIS, and RCu-ZIS. The large arc radius of ZIS is consistent with its significant interfacial charge transfer resistance and tardy photocarrier migration dynamics. In comparison, the arc radius of Cu-ZIS displays an obvious depression, implying improved electron conductivity with Cu atom doping. Meanwhile, it can be observed that the arc radius of RCu-ZIS presents an enlargement in comparison to that of Cu-ZIS, but is still smaller than that of pristine ZIS. The changed electron conductivity may relate to the changed electronic structure in RCu-ZIS.

3.4. Photocatalytic mechanism and H₂ evolution activity study

As mentioned above, the isolated Cu SAs, Cu doping atoms, S vacancies, and Cu/In/S vacancies clusters result in some local electric fields with different states of charge in RCu-ZIS. Specifically, as shown in Fig. 7a, S vacancies and the isolated Cu SAs result in electron donor states in RCu-ZIS, meanwhile, the Cu doping atoms and Cu/In/S vacancies clusters introduce electron acceptor states. Therefore, under processive visible-light illumination, electrons in the VB of RCu-ZIS were excited to become energized electrons, a part photogenerated electrons accompanied with the photoinduced electrons excited from the donating levels of S vacancies and isolated Cu SAs can jump to the CB. Meanwhile, another part of electrons in the VB of RCu-ZIS could be captured by the acceptable levels of Cu doping atoms and Cu/In/S vacancies clusters and then excited to the CB of RCu-ZIS. With such multiple excitation and transfer passage of photocarriers, extensive photogenerated electrons would be resolved and participate in the reduction reaction of H$^+$ to H₂. Finally, a significantly enhanced photocatalytic H₂ evolution performance would be realized.

To verify the benefits of the above photocatalytic reaction mechanism, photocatalytic H₂ evolution experiments of the as-prepared photocatalysts were carried out. As shown in Fig. 7b, under visible light irradiation, pristine ZIS photocatalyst presents a feeble H₂ evolution rate of 2.42 mmol·g^{-1}·h^{-1}. With Cu$^+$ doping, the H₂ production efficiency of Cu-ZIS improves rapidly, and when the additional amount of Cu$^+$ is adjusted to 0.04 mmol, the H₂ evolution rate reaches the highest of 23.23 mmol·g^{-1}·h^{-1}. Furtherly, the H₂ production rate of RCu-ZIS photocatalysts further increases, revealing the positive action of Cu$^+$ leaching on optimizing photocatalytic activity. It is noteworthy that the optimized RCu-ZIS exhibited the highest H₂ evolution rate of 70.58 mmol·g^{-1}·h^{-1} (Fig. 7c). As observed more intuitively from Fig. 7d, all RCu-ZIS photocatalysts exhibit a higher H₂ evolution rate than Cu-ZIS. Moreover, H₂ evolution over the optimized RCu-ZIS photocatalyst was tested under different addition amounts. As exhibited in Fig. 7e, with the amount of RCu-ZIS increasing, H₂ evolution per unit time (rate) improves accordingly, and the plateau value happens by adding 30 mg of photocatalyst (1.623 mmol·h^{-1}). Further increase of photocatalyst can only bring about inappreciable H₂ evolution rate enhancement (50 mg: 1.655 mmol·h^{-1}). Such observation suggests that the photonic absorbance over RCu-ZIS reaches saturation when the addition of RCu-ZIS is 30 mg. As one of the direct indicators of efficient photocatalyst, apparent quantum efficiency (AQE) was tested by adding 30 mg of RCu-ZIS. According to the H₂ evolution rate and light power at different monochromatic light (Table S6), the AQE values of the RCu-ZIS photocatalyst were determined to be 51% (380 nm), 12.24% (420 nm), 2.92% (500 nm), and 1.09% (600 nm) (Fig. 7f). The detailed calculation can be found in Supporting Information. The high AQE value further indicates the efficient photocatalyst H₂ evolution performance of RCu-

ZIS. Fig. 7g displays the cycling stability test over RCu-ZIS. As observed, only a slight decrease in H₂ evolution can be detected during successive six times of cycles, revealing the good stability of RCu-ZIS. To reveal the origin of the robust stability over RCu-ZIS, SEM, TEM, and EPR of the RCu-ZIS after stability tests were carried out. As shown in Fig, S12, after 6 times reuses, RCu-ZIS still keeps the morphology of the microsphere composed of numerous ultrathin nanosheets, suggesting its robust structural stability. Besides that, the EPR signal over the RCu-ZIS after the stability test decreased slightly but was still prominent, revealing that the ample defect structure didn't annihilate in RCu-ZIS (Fig. S13). The above favorable H₂ evolution activity and AQE of RCu-ZIS are far beyond the majority of representative ZnIn₂S₄ photocatalysts modified by metal doping or decorating (Fig. 7h and Table S7).

4. Conclusions

In summary, for the first time, an ingenious low-valent cation doping and leaching strategy was developed for constructing isolated Cu SAs, Cu doping atoms, S vacancies, and Cu/In/S vacancies clusters co-modified ZnIn₂S₄ photocatalyst. Favored by the different charge states of isolated Cu SAs and multiple defect sites, some local electric fields were formed in RCu-ZIS, in which the isolated Cu SAs and S vacancies served as electrons donating centers, while Cu doping atoms and Cu/In/S vacancies clusters acted as electrons accepting centers, which synergistically promoted the separation and transfer behavior of photocarriers in RCu-ZIS, and finally contributed to multitudinous photogenerated electrons that can participate in H₂ evolution reaction. As a result, the optimized RCu-ZIS presented a high visible-light-driven H₂ evolution rate of 70.58 mmol·g^{-1}·h^{-1}, 29.2 times the pristine ZIS. Meanwhile, a high AQE of 12.24% at 420 nm and favorable stability during successive six times of uses were achieved. This work offers an unsophisticated, practical, and easy-to-scale-up strategy for realizing the effective modulation of microstructure and electronic state, and donates an available pathway to boost photocatalytic H₂ evolution activity.

CRediT authorship contribution statement

Li Zhen-Jiang: Conceptualization, Data curation, Funding acquisition, Project administration, Supervision, Validation, Writing – review & editing. **Meng Alan:** Conceptualization, Funding acquisition, Project administration, Supervision, Writing – review & editing. **Huang Jian-feng:** Formal analysis, Resources. **Wang Xianghu:** Data curation, Methodology, Software, Visualization. **Shi Tianyu:** Formal analysis, Methodology, Software, Visualization. **Wang Lei:** Conceptualization, Resources. **Li Guicun:** Conceptualization, Resources. **Wang Xuehua:** Conceptualization, Data curation, Formal analysis, Methodology, Writing – original draft.

Declaration of Competing Interest

The authors declare that they have no known competing financial interests or personal relationships that could have appeared to influence the work reported in this paper.

Data Availability

Data will be made available on request.

Acknowledgments

Appendix A. Supporting information

Supplementary data associated with this article can be found in the online version at doi:10.1016/j.apcatb.2024.123807.

References

[1] H. Nishiyama, T. Yamada, M. Nakabayashi, Y. Maehara, M. Yamaguchi, Y. Kuromiya, Y. Nagatsuma, H. Tokudome, S. Akiyama, T. Watanabe, R. Narushima, S. Okunaka, N. Shibata, T. Takata, T. Hisatomi, K. Domen, Photocatalytic solar hydrogen production from water on a 100-m^2 scale, Nature 598 (2021) 304–307.

[2] H.S. Moon, K.-C. Hsiao, M.-C. Wu, Y. Yun, Y.-J. Hsu, K. Yong, Spatial separation of cocatalysts on Z-scheme organic/inorganic heterostructure hollow spheres for enhanced photocatalytic H$_2$ evolution and in-depth analysis of the charge-transfer mechanism, Adv. Mater. 35 (2023) 2370025.

[3] X. Mu, L. Li, Photocatalytic hydrogen production from alkanes, Nat. Energy 7 (2022) 1011–1012.

[4] S. Liu, X. Zhou, C. Yang, C. Wei, Y. Hu, Cu atoms on UiO-66-NH$_2$/ZnIn$_2$S$_4$ nanosheets enhance photocatalytic performance for recovering hydrogen energy from organic wastewater treatment, Appl. Catal. B: Environ. 330 (2023) 122572.

[5] M. Gao, F. Tian, X. Zhang, Z. Chen, W. Yang, Y. Yu, Improved plasmonic hot-electron capture in Au nanoparticle/polymeric carbon nitride by Pt single atoms for broad-spectrum photocatalytic H$_2$ evolution, Nano-Micro Lett. 15 (2023) 129.

[6] Y. Wang, Y. Qin, N. Denisov, H. Kim, Z. Bad'ura, B.B. Sarma, P. Schmuki, Reactive deposition versus strong electrostatic adsorption (SEA): a key to highly active single atom co-catalysts in photocatalytic H$_2$ generation, Adv. Mater. 35 (2023) 2211814.

[7] S. Li, S. Wang, J. He, K. Li, Y. Xu, M. Wang, S. Zhao, Y. Wang, X. Li, X. Zhong, J. Wang, Chromium-doped nickel oxide and nickel nitride mediate selective electrocatalytic oxidation of sterol intermediates coupled with H$_2$ evolution, Angew. Chem., Int. Ed. 62 (2023) e202306553.

[8] W. Wang, Y. Song, C. Ke, Y. Li, Y. Liu, C. Ma, Z. Wu, J. Qi, K. Bao, L. Wang, J. Wu, S. Jiang, J. Zhao, C.-S. Lee, Y. Chen, G. Luo, Q. He, R. Ye, Filling the gap between heteroatom doping and edge enrichment of 2D electrocatalysts for enhanced hydrogen evolution, ACS Nano 17 (2023) 1287–1297.

[9] Y. Zhang, Y. Li, X. Xin, Y. Wang, P. Guo, R. Wang, B. Wang, W. Huang, A.J. Sobrido, X. Li, Internal quantum efficiency higher than 100% achieved by combining doping and quantum effects for photocatalytic overall water splitting, Nat. Energy 8 (2023) 504–514.

[10] Y. Liu, H. Tan, Y. Wei, M. Liu, J. Hong, W. Gao, S. Zhao, S. Zhang, S. Guo, Cu$_2$O/2D COFs core/shell nanocubes with antiphotocorrosion ability for efficient photocatalytic hydrogen evolution, ACS Nano 17 (2023) 5994–6001.

[11] D. Liu, S. Chen, Y. Zhang, R. Li, T. Peng, Modulating the bridging units of carbon nitride for highly efficient charge separation and visible-light-responsive photocatalytic H$_2$ evolution, Appl. Catal. B: Environ. 333 (2023) 122805.

[12] T. Wang, L. Zhang, J. Wu, M. Chen, S. Yang, Y. Lu, P. Du, Few-layer fullerene network for photocatalytic pure water splitting into H$_2$ and H$_2$O$_2$, Angew. Chem., Int. Ed. (2023) e202311352.

[13] R. Shen, N. Li, C. Qin, X. Li, P. Zhang, X. Li, J. Tang, Heteroatom- and bonded Z-scheme channels-modulated ultrafast carrier dynamics and exciton dissociation in covalent triazine frameworks for efficient photocatalytic hydrogen evolution, Adv. Funct. Mater. 33 (2023) 2301463.

[14] Z. Li, T. Deng, S. Ma, Z. Zhang, G. Wu, J. Wang, Q. Li, H. Xia, S.-W. Yang, X. Liu, Three-component donor−π−acceptor covalent–organic frameworks for boosting photocatalytic hydrogen evolution, J. Am. Chem. Soc. 145 (2023) 8364–8374.

[15] D. Zhao, Y. Wang, C.-L. Dong, Y.-C. Huang, J. Chen, F. Xue, S. Shen, L. Guo, Boron-doped nitrogen-deficient carbon nitride-based Z-scheme heterostructures for photocatalytic overall water splitting, Nat. Energy 6 (2021) 388–397.

[16] Y. Akinaga, T. Kawawaki, H. Kameko, Y. Yamazaki, K. Yamazaki, Y. Nakayasu, K. Kato, Y. Tanaka, A.T. Hanindriyo, M. Takagi, T. Shimazaki, M. Tachikawa, A. Yamakata, Y. Negishi, Metal single-atom cocatalyst on carbon nitride for the photocatalytic hydrogen evolution reaction: effects of metal species, Adv. Funct. Mater. 33 (2023) 2370202.

[17] S. Guo, Y. Ji, Y. Li, H. Li, P. An, J. Zhang, J. Yan, S. Liu, T. Ma, Amorphous quantum dots co-catalyst: Defect level induced solar-to-hydrogen production, Appl. Catal. B: Environ. 330 (2023) 122583.

[18] J. Ding, Z. Teng, X. Su, K. Kato, Y. Liu, T. Xiao, W. Liu, L. Liu, Q. Zhang, X. Ren, J. Zhang, Z. Chen, O. Teruhisa, A. Yamakata, H. Yang, Y. Huang, B. Liu, Y. Zhai, Asymmetrically coordinated cobalt single atom on carbon nitride for highly selective photocatalytic oxidation of CH$_4$ to CH$_3$OH, Chem 9 (2023) 1017–1035.

[19] J. Xing, J.F. Chen, Y.H. Li, W.T. Yuan, Y. Zhou, L.R. Zheng, H.F. Wang, P. Hu, Y. Wang, H.J. Zhao, Y. Wang, H.G. Yang, Stable isolated metal atoms as active sites for photocatalytic hydrogen evolution, Chem. Eur. J. 20 (2014) 2138–2144.

[20] H. Huang, H. Song, J. Kou, C. Lu, J. Ye, Atomic-level insights into surface engineering of semiconductors for photocatalytic CO$_2$ reduction, J. Energy Chem. 67 (2023) 309–341.

[21] T. Wang, L. Chen, C. Chen, M. Huang, Y. Huang, S. Liu, B. Li, Engineering catalytic interfaces in Cu$^{\delta+}$/CeO$_2$-TiO$_2$ photocatalysts for synergistically boosting CO$_2$ reduction to ethylene, ACS Nano 16 (2022) 2306–2318.

[22] K. Zhang, M. Dan, J. Yang, F. Wu, L. Wang, H. Tang, Z.-Q. Liu, Surface energy mediated sulfur vacancy of ZnIn$_2$S$_4$ atomic layers for photocatalytic H$_2$O$_2$ production, Adv. Funct. Mater. 33 (2023) 2302964.

[23] S. Zhang, Z. Zhang, Y. Si, B. Li, F. Deng, L. Yang, X. Liu, W. Dai, S. Luo, Gradient hydrogen migration modulated with self-adapting S vacancy in copper-doped ZnIn$_2$S$_4$ nanosheet for photocatalytic hydrogen evolution, ACS Nano 15 (2021) 15238–15248.

[24] G. Kresse, J. Furthmüller, Efficiency of ab-initio total energy calculations for metals and semiconductors using a plane-wave basis set, Comput. Mater. Sci. 6 (1996) 15–50.

[25] M.D. Segall, J.D.L. Philip, M.J. Probert, C.J. Pickard, P.J. Hasnip, S.J. Clark, M.C. Payne, First-principles simulation: ideas, illustrations and the CASTEP code, J. Phys.: Condens. Matter 14 (2002) 2717.

[26] P.E. Blöchl, Projector augmented-wave method, Phys. Rev. B 50 (1994) 17953–17979.

[27] J.P. Perdew, K. Burke, M. Ernzerhof, Generalized gradient approximation made simple, Phys. Rev. Lett. 77 (1996) 3865–3868.

[28] Z. Wang, M. Tripathi, Z. Golsanamlou, P. Kumari, G. Lovarelli, F. Mazziotti, D. Logoteta, G. Fiori, L. Sementa, G.M. Marega, H.G. Ji, Y. Zhao, A. Radenovic, G. Iannaccone, A. Fortunelli, A. Kis, Substitutional p-type doping in NbS$_2$–MoS$_2$ lateral heterostructures Grown by MOCVD, Adv. Mater. 35 (2023) 2209371.

[29] N.-Y. Park, S.-B. Kim, M.-C. Kim, S.-M. Han, D.-H. Kim, M.-S. Kim, Y.-K. Sun, Mechanism of doping with high-valence elements for developing Ni-Rich cathode materials, Adv. Energy Mater. (2023) 2301530.

[30] X. Wang, X. Wang, J. Huang, S. Li, A. Meng, Z. Li, Interfacial chemical bond and internal electric field modulated Z-scheme S$_v$-ZnIn$_2$S$_4$/MoSe$_2$ photocatalyst for efficient hydrogen evolution, Nat. Commun. 12 (2021) 4112.

[31] Y. Li, B. Sun, H. Lin, Q. Ruan, Y. Geng, J. Liu, H. Wang, Y. Yang, L. Wang, K. Chiu Tam, Efficient visible-light induced H$_2$ evolution from T-Cd$_x$Zn$_{1−x}$S/defective MoS$_2$ nano-hybrid with both bulk twinning homojunctions and interfacial heterostructures, Appl. Catal. B: Environ. 267 (2020) 118702.

[32] C. Han, G. Han, S. Yao, L. Yuan, X. Liu, Z. Cao, A. Mannodi-Kanakkithodi, Y. Sun, Defective ultrathin ZnIn$_2$S$_4$ for photoreductive deuteration of carbonyls using D$_2$O as thedeuterium source, Adv. Sci. 9 (2022) 2103408.

[33] Z. Hou, Z. Sun, C. Cui, D. Zhu, Y. Yang, T. Zhang, Ru coordinated ZnIn$_2$S$_4$ triggers local lattice-strain engineering to endow high-efficiency electrocatalyst for advanced Zn-air batteries, Adv. Funct. Mater. 32 (2022) 2110572.

[34] X. Shi, W. Dai, Xa Dong, Q. Ren, J. Sheng, F. Dong, Dual Cu and S vacancies boost CO$_2$ photomethanation on Cu$_{1.95}$S$_{1−x}$: Vacancy-regulated selective photocatalysis, Appl. Catal. B: Environ. 339 (2023) 123147.

[35] X. Jia, Y. Lu, K. Du, H. Zheng, L. Mao, H. Li, Z. Ma, R. Wang, J. Zhang, Interfacial mediation by Sn and S Vacancies of p-SnS/n-ZnIn$_2$S$_4$ for enhancing photocatalytic hydrogen evolution with new scheme of type-I heterojunction, Adv. Funct. Mater. (2023) 2304072.

[36] Y. Wang, M. Liu, C. Wu, J. Gao, M. Li, Z. Xing, Z. Li, W. Zhou, Hollow nanoboxes Cu$_{2−x}$S@ZnIn$_2$S$_4$ core-shell S-scheme heterojunction with broad-spectrum response and enhanced photothermal-photocatalytic performance, Small (2022) 2202544.

[37] K. Wang, Y. Zhu, M. Gu, Z. Hu, Y.-C. Chang, C.-W. Pao, Y. Xu, X. Huang, A Derivative of ZnIn$_2$S$_4$ nanosheet supported Pd boosts selective CO$_2$ hydrogenation, Adv. Funct. Mater. 33 (2023) 2215148.

[38] Y. Li, B. Sun, H. Lin, Q. Ruan, Y. Geng, J. Liu, H. Wang, Y. Yang, L. Wang, K.C. Tam, Corrigendum to "Efficient visible-light induced H$_2$ evolution from T-Cd$_x$Zn$_{1−x}$S/defective MoS$_2$ nano-hybrid with both bulk twinning homojunctions and interfacial heterostructures" [Appl. Catal. B: Environ. 267 (2020) 118702], Appl. Catal. B: Environ. 271 (2020) 118866.

[39] T. Tian, T. Jin, N. Guo, H. Li, Y. Han, Y. Yuan, CdS/ethylenediamine nanowires 3D photocatalyst with rich sulfur vacancies for efficient syngas production from CO$_2$ photoreduction, Appl. Catal. B: Environ. 308 (2022) 121227.

[40] S. Zhang, X. Liu, S. Liu, L. Luo, L. Wang, T. Cai, Y. Zeng, J. Yuan, W. Dong, Y. Pei, Y. Liu, MoS$_2$ quantum dot growth induced by S vacancies in a ZnIn$_2$S$_4$ monolayer: atomic-level heterostructure for photocatalytic hydrogen production, ACS Nano 12 (2018) 751–758.

[41] H. Zhou, D. Zhang, H. Xie, Y. Liu, C. Meng, P. Zhang, F. Fan, R. Li, C. Li, Modulating oxygen vacancies in lead chromate for photoelectrocatalytic water splitting, Adv. Mater. 35 (2023) 2300914.

[42] L. Wang, Z. Xu, C.-H. Kuo, J. Peng, F. Hu, L. Li, H.-Y. Chen, J. Wang, S. Peng, Stabilizing low-valence single atoms by constructing metalloid tungsten carbide supports for efficient hydrogen oxidation and evolution, Angew. Chem. Int. Ed. 62 (2023) e202311937.

[43] X. Cheng, B. Xiao, Y. Chen, Y. Wang, L. Zheng, Y. Lu, H. Li, G. Chen, Ligand charge donation–acquisition balance: a unique strategy to boost single Pt atom catalyst mass activity toward the hydrogen evolution reaction, ACS Catal. 12 (10) (2022) 5970–5978.

[44] Y. Wu, Q. Wu, Q. Zhang, Z. Lou, K. Liu, Y. Ma, Z. Wang, Z. Zheng, H. Cheng, Y. Liu, Y. Dai, B. Huang, P. Wang, An organometal halide perovskite supported Pt single-atom photocatalyst for H$_2$ evolution, Energy Environ. Sci. 15 (2022) 1271–1281.

[45] M. Wang, S. Xu, Z. Zhou, C.-L. Dong, X. Guo, J.-L. Chen, Y.-C. Huang, S. Shen, Y. Chen, L. Guo, C. Burda, Atomically dispersed janus nickel sites on red phosphorus for photocatalytic overall water splitting, Angew. Chem., Int. Ed. 61 (2022) e202204711.

[46] S. Zhang, Z. Zhang, Y. Si, B. Li, F. Deng, L. Yang, X. Liu, W. Dai, S. Luo, Gradient hydrogen migration modulated with self-adapting S vacancy in copper-doped ZnIn$_2$S$_4$ nanosheet for photocatalytic hydrogen evolution, ACS Nano 15 (2021) 15238–15248.

[47] M. Tamtaji, S. Cai, W. Wu, T. Liu, Z. Li, H.-Y. Chang, P.R. Galligan, S.-i Iida, X. Li, F. Rehman, K. Amine, W.A. Goddard, Z. Luo, Single and dual metal atom catalysts for enhanced singlet oxygen generation and oxygen reduction reaction, J. Mater. Chem. A 11 (2023) 7513–7525.

[48] P. Wang, Z. Shen, Y. Xia, H. Wang, L. Zheng, W. Xi, S. Zhan, Atomic insights for optimum and excess doping in photocatalysis: a case study of few-layer Cu-ZnIn$_2$S$_4$, Adv. Funct. Mater. 29 (2019) 1807013.

[49] K. Jiang, M. Luo, Z. Liu, M. Peng, D. Chen, Y.-R. Lu, T.-S. Chan, F.M.F. de Groot, Y. Tan, Rational strain engineering of single-atom ruthenium on nanoporous MoS$_2$ for highly efficient hydrogen evolution, Nat. Commun. 12 (2021) 1687.

[50] D. Zhou, X. Xue, X. Wang, Q. Luan, A. Li, L. Zhang, B. Li, W. Dong, G. Wang, C. Hou, Ni, In co-doped ZnIn$_2$S$_4$ for efficient hydrogen evolution: modulating charge flow and balancing H adsorption/desorption, Appl. Catal. B: Environ. 310 (2022) 121337.

[51] Y. Zhao, Y. Zhao, R. Shi, B. Wang, G.I.N. Waterhouse, L.-Z. Wu, C.-H. Tung, T. Zhang, Tuning oxygen vacancies in ultrathin TiO$_2$ nanosheets to boost photocatalytic nitrogen fixation up to 700 nm, Adv. Mater. 31 (2019) 1806482.

[52] M. Dong, P. Zhou, C. Jiang, B. Cheng, J. Yu, First-principles investigation of Cu-doped ZnS with enhanced photocatalytic hydrogen production activity, Chem. Phys. Lett. 668 (2017) 1–6.

[53] W. Jiang, H. Loh, B.Q.L. Low, H. Zhu, J. Low, J.Z.X. Heng, K.Y. Tang, Z. Li, X. J. Loh, E. Ye, Y. Xiong, Role of oxygen vacancy in metal oxides for photocatalytic CO$_2$ reduction, Appl. Catal. B: Environ. 321 (2023) 122079.

[54] Y. Liu, C. Chen, Y. He, Z. Zhang, M. Li, C. Li, X.-B. Chen, Y. Han, Z. Shi, Rich indium-vacancies In$_2$S$_3$ with atomic p–n homojunction for boosting photocatalytic multifunctional properties, Small 18 (2022) 2201556.

[55] B. Hu, M. Hu, Q. Guo, K. Wang, X. Wang, In-vacancy engineered plate-like In(OH)$_3$ for effective photocatalytic reduction of CO$_2$ with H$_2$O vapor, Appl. Catal. B: Environ. 253 (2019) 77–87.

[56] X. Shi, C. Dai, X. Wang, J. Hu, J. Zhang, L. Zheng, L. Mao, H. Zheng, M. Zhu, Protruding Pt single-sites on hexagonal ZnIn$_2$S$_4$ to accelerate photocatalytic hydrogen evolution, Nat. Commun. 13 (2022) 1287.

[57] X. Wang, X. Wang, W. Tian, A. Meng, Z. Li, S. Li, L. Wang, G. Li, High-energy ball-milling constructing P-doped g-C$_3$N$_4$/MoP heterojunction with MoN bond bridged interface and Schottky barrier for enhanced photocatalytic H2 evolution, Appl. Catal. B: Environ. 303 (2022) 120933.

[58] P. Wang, Z. Shen, Y. Xia, H. Wang, L. Zheng, W. Xi, S. Zhan, Atomic insights for optimum and excess doping in photocatalysis: a case study of few-layer Cu-ZnIn$_2$S$_4$, Adv. Funct. Mater. 29 (2019) 1807013.

[59] L. Zhang, Z. Wang, C. Hu, B. Shi, Enhanced photocatalytic performance by the synergy of Bi vacancies and Bi^0 in Bi^0-Bi$_{2.8}$MoO$_6$, Appl. Catal. B: Environ. 257 (2019) 117785.

[60] Z. Zhao, Z. Wang, J. Zhang, C. Shao, K. Dai, K. Fan, C. Liang, Interfacial chemical bond and oxygen vacancy-enhanced In$_2$O$_3$/CdSe-DETA S-scheme heterojunction for photocatalytic CO$_2$ conversion, Adv. Funct. Mater. (2023) 2214470.

[61] X. Li, J. Hu, T. Yang, X. Yang, J. Qu, C.M. Li, Efficient photocatalytic H$_2$-evolution coupled with valuable furfural-production on exquisite 2D/2D LaVO$_4$/g-C$_3$N$_4$ heterostructure, Nano Energy 92 (2022) 106714.

[62] R. Shi, H.-F. Ye, F. Liang, Z. Wang, K. Li, Y. Weng, Z. Lin, W.-F. Fu, C.-M. Che, Y. Chen, Interstitial P-doped CdS with long-lived photogenerated electrons for photocatalytic water splitting without sacrificial agents, Adv. Mater. 30 (2018) 1705941.

[63] G. Ren, S. Liu, Z. Li, H. Bai, X. Hu, X. Meng, Highly Selective Photocatalytic reduction of CO$_2$ to CO over Ru-modified Bi$_2$MoO$_6$, Sol. RRL 6 (2022) 2200154.

[64] T. Liu, P. Li, N. Yao, G. Cheng, S. Chen, W. Luo, Y. Yin, CoP-doped MOF-based electrocatalyst for pH-universal hydrogen evolution reaction, Angew. Chem. Int. Ed. 58 (2019) 4679–4684.